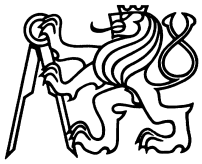

České vysoké učení technické v Praze
Fakulta jaderná a fyzikálně inženýrská

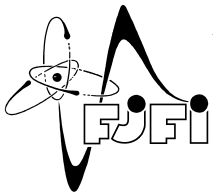

L-H přechod v tokamakovém plazmatu

L-H transition in tokamak plasma

Výzkumný úkol
Research assignment

Autor: Ondřej Grover

Vedoucí práce: Ing. Martin Hron, Ph.D.

Akademický rok: 2015/2016

Contents

1 Introduction

In the previous thesis [4] the oscillations occasionally observed during the L-H (and even H-L) transition in the COMPASS tokamak were discussed as possibly being limit cycle oscillations (LCO) characteristic of predator-prey dynamics that can arise during the L-H transition in the so called I-mode (intermediary mode)[8].

The main focus of this work was to continue with the characterization of the LCO-like oscillations shown in terms of the predator-prey-like dynamics where the level of fluctuations caused presumably by turbulence and the strength of the shearing E_r field causing a decorrelation of the turbulence structures. In the previous thesis there was an attempt to estimate E_r with an existing probe head of the horizontal midplane reciprocating manipulator. That attempt was unsuccessful presumably because of a nearly non-existent radial separation of the probes. In this work the design of modified and new probe heads and their tests are described in section 4.

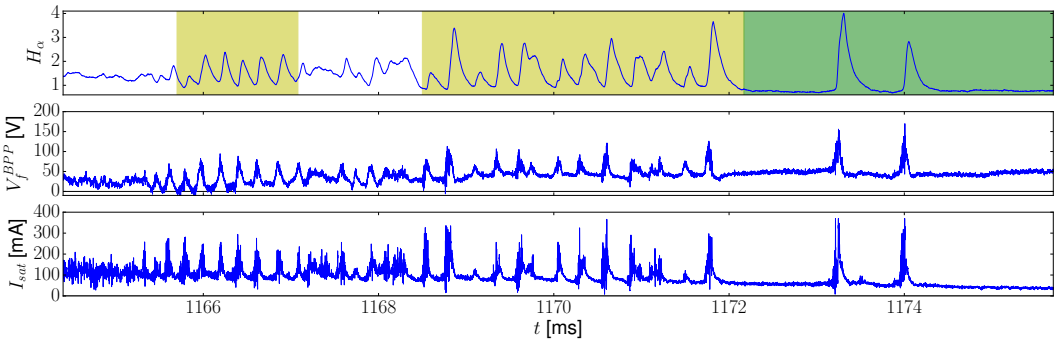

Figure 1: LCO-like oscillations observed in discharge 9617 during the L-H transition. The suspected I-mode is highlighted by yellow regions.

While the final design appears to successfully reconstruct E_r, there have been no dedicated experiments with this new design that would enable measurements of the LCO-like oscillations. For this reason other methods have been used to characterize these oscillations through other means. The spectral features of these oscillations, namely their magnetic mode and bicoherence are described in section 2. There was also an attempt to reconstruct E_r using a method similar to conditional averaging described in section 3.

2 Spectral analysis of data with LCO-like structures

While spectral analysis of signals may not offer direct evidence of predator-prey dynamics, it can give supporting evidence in the form of spectral characteristics associated with LCO based on observations in other experiments. The most prominent is the coherence and bicoherence (i.e. phase stability) of magnetic and other spectral modes at the frequency associated with LCO.

Usually the coherence is calculated by taking the Fourier transform of non-overlapping (otherwise they might be statistically correlated) segments of the signals and the averaging is performed over these segments. However, this is only applicable if

1. the time-span of the occurrence of the studied event is long enough to be split into a statistically significant number of segments

2. the frequency of the studied mode is well resolved by the frequency resolution given by the length of the window $f_{RES} = \frac{f_{nyq}}{N}$ where N is the length of the window and f_{nyq} the Nyquist frequency (half of the sampling frequency)

The LCO-like oscillations under investigation have a frequency ~ 3 kHz which would require a frequency resolution at least ~ 1 kHz which hen results in a required length of the window $\sim 10^3$ with a sampling frequency in the order of MHz. This would result in windows with a time-span of $\sim 1ms$. However, the time-span of the oscillations during the transition itself has several a length of ms at most which would result only in several segments over which the average could be taken. Therefore, a different method which does not need discrete segments is required.

One option is to use the wavelet transform with the complex Morlet (a.k.a. Gabor) wavelet which decomposes the signal into the basis of functions $\exp(-(t\omega\alpha)^2)\exp(i\omega t)$ instead of the Fourier function basis $\exp(i\omega t)$. The complex Morlet wavelets are therefore a windowed version of the Fourier basis functions with the width of the Gaussian window determined by the factor α. Their frequency response is that of a band-pass filter with a Gaussian profile with the width of the profile inversely proportional to the mean frequency. However, unlike the Fourier basis they are not orthogonal in general. Nevertheless, a choice of an exponential scale of frequencies $\omega_k = \omega_0 2^k$ results in an orthogonal basis. Such a basis gives detailed information about lower frequencies and less about higher frequencies (where the Gaussian windows in the frequency domain would overlap). This fact is not significant for the low frequency oscillations under investigation. Nevertheless, the wavelet functions provide a so called constant $Q = f_{res}t_{res}$ transform where the product of the frequency and time resolutions remain constant. The decomposition into this basis can be seen as a partitioning of the time-frequency space into rectangles of constant surfaces but exponentially increasing/decreasing sides.

The signal is decomposed into the wavelet basis by cross-correlating each basis function with the signal which results in a both time and frequency resolved spectra $\hat{W}(\tau, \omega)$, because at each time lag τ the correlation with a wavelet function with a mean frequency ω gives the power of the respective frequency bundle in the Gaussian time window around the given time lag. The advantage of this method lies in the fact that the correlation can be performed in the frequency domain by multiplying the frequency transform of the signal with the band-pass Gaussian windows. The frequency transform is therefore taken over the whole signal under investigation which greatly increases the frequency resolution of the transform.

One disadvantage of the correlation approach is that boundary effects arise due to the finite length of the signal. The influence of the boundary effects is larger for lower frequencies due to the larger Gaussian window. The approximate effect boundary is given as a so called cone of influence (COI) and this area is darkened in graphs below.

2.1 Magnetic modes

One of the characteristics of LCO-like structures is their $n = 0$ toroidal mode number, i.e. they are uniform in the toroidal direction [3]. The mode number can be found by inspecting the frequency characteristic of the signal from the magnetic Mirnov coils which pick up perturbations of the magnetic field. Any mode with a characteristic frequency f which influences

the magnetic field is likely to have a distinctive impact on the frequency spectrum of the measured magnetic signals. If the mode is stationary, it should appear as two coherent frequency components f on spatially separated magnetic coils, i.e. the phase shift $\Delta\varphi$ between the two frequency components $\hat{x}(f)$, $\hat{y}(f)$ should appear constant over consecutive time segments. Normalized coherence is then defined as

$$C_{xy} = \frac{\langle|\hat{x}(f)\hat{y}(f)|^2\rangle}{PSD_x PSD_y} \tag{1}$$

and takes on values from -1 to 1. $PSD_x = \langle|\hat{x}(f)|^2\rangle$ is the power-spectral density of the given frequency component, i.e. a measure of how much of the signal is determined by that frequency component. If the phase difference between the frequency components is constant in the range of the time segments, the averaging will return a non-zero value. If the phase shift is random (they are not coherent), it will average out to 0. In effect it presents a frequency dependent correlation coefficient. For modes considered coherent (e.g. with $C_{xy} > 0.7$) the mode number can be estimated as $n = \frac{\Delta\varphi}{\Delta\phi}$ with $\Delta\phi$ being the toroidal angle between the two Mirnov coils.

As was described above, the LCO-like structures under investigation require a different method than the standard averaging over consecutive segments and therefore wavelet cross-coherence analysis was used. The frequency spectra $\hat{x}(f,\tau)$ also have a time resolution and the averaging is performed by convolution with Gaussian windows (the absolute value of the wavelet basis functions) corresponding to each wavelet basis function. Therefore, shorter averaging windows are used for higher frequencies where the spectral characteristics may change more rapidly than at lower frequencies which provides an optimal averaging filter.

The wavelet cross-coherence calculation was performed using the `pycwt` Python package which is based on [6]. The package was modified to optionally use the `FFTW` library which can quickly perform the Fourier transform on signals of arbitrary length (no only on power of 2, 3, 5 as most radix-based FFT algorithms) which reduced the computation time and the memory requierements (due to zero-padding to power of 2), these modifications were later merged into the original package.

Figure 2 shows a clear $n = 0$ coherent mode at the frequency of the LCO-like oscillations.

2.2 Bicoherence

Bicoherence is a measure of the presence of a three-wave interaction, i.e. of three modes f_i which satisfy $f_1 = f_2 + f_3$. Such an interaction is common in systems with a quadratic nonlinearity which can be seen e.g. by substituting variables in quadratic term by their Fourier transforms

$$\begin{aligned} x \cdot y &= \int \hat{x}\exp(-if_1 t)df_1 \int \hat{y}\exp(-if_2 t)df_2 = \int\int \hat{x}\hat{y}\exp(-i(f_1+f_2)t)df_1 df_2 = \\ &= \int \left(\int \hat{x}(f')\hat{y}(f-f')\right) df' \exp(-ift)df \end{aligned}$$

If the three modes interact, their phases are locked together $\phi_1 - \phi_2 - \phi_3 = \text{const}$. This property is similar to coherence where two modes had a constant phase phase difference, but for three modes it is called bicoherence and three spectral components are inspected. Bicoherence $B_{xy}(f_1, f_2)$ is then defined[5] in a similar fashion as in (1), but the numerator features a term $|\langle\hat{x}(f_1+f_2)\hat{y}(f_1)\hat{y}(y_2)\rangle|^2$ which represents the averaging of the phase difference between the

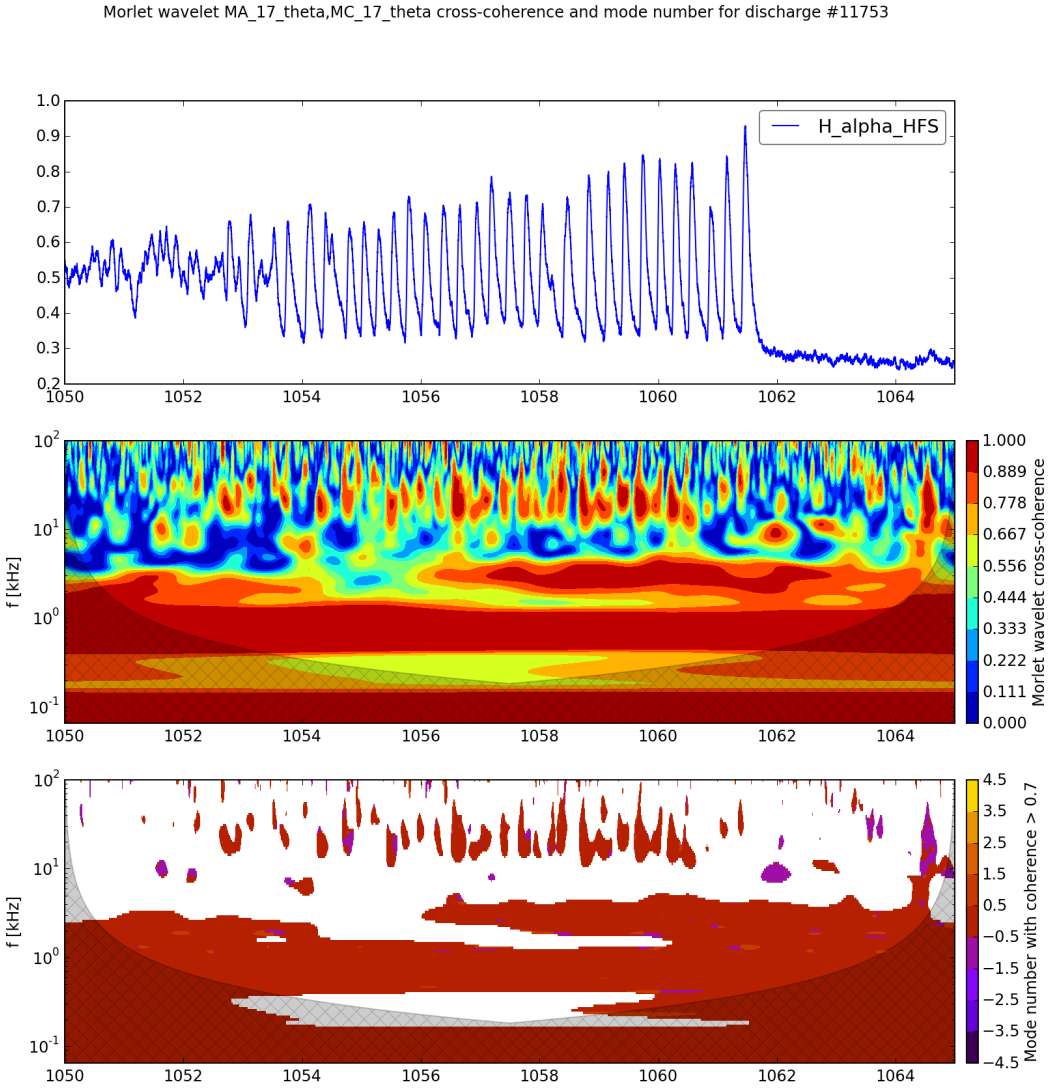

Figure 2: Wavevlet cross-coherence analysis of poloidal Mirnov copils 17A and 17C during the L-H transition in discharge 11753. The LCO-like oscillations at frequency ~ 3 kHz display a clear coherent $n = 0$ mode.

three modes. The denominator normalizes bicoherence to $\langle -1, 1 \rangle$ as before and contains the terms $\langle |\hat{y}(f)|^2 \rangle \langle |\hat{y}(f_2)\hat{y}(f_2)|^2 \rangle$.

The definition makes it possible to calculate auto-bicoherence B_{xx} which requires only one signal which may already show presence of quadratic nonlinearlities in the dynamics of the system. When $B_{xx}(f_1, f_2)$ is put into a color plot a three-mode interaction will show up as three points at $[f_1, f_2]$, $[-f_1, f_1 + f_2]$, $[-f_2, f_1 + f_2]$. If the coupling strength of the modes varies with within the averaging sample, the values of B_{xx} will be different at these points.

Bicoherence was calculated for the BPP1 signal in discharge 9617 for a time slice where the LCO-like oscillations occurred. Wavelet spectrum was used instead of a Fourier spectrum which is likely better suited to detect intermittent mode coupling often seen in turbulence dynamics [5] and it also offers a higher time resolution at lower frequencies with such short

signal time-spans. A clear bicoherence at the oscillations frequency ~ 3 kHz is seen and this mode seems to interact with a broad band of other modes which reproduces results from [8]. The interaction with modes of higher frequencies likely continues to higher frequencies, however, the unoptimized algorithm did not permit their inclusion due to memory limitations. In the future the algorithm could be improved by using fewer temporary arrays.

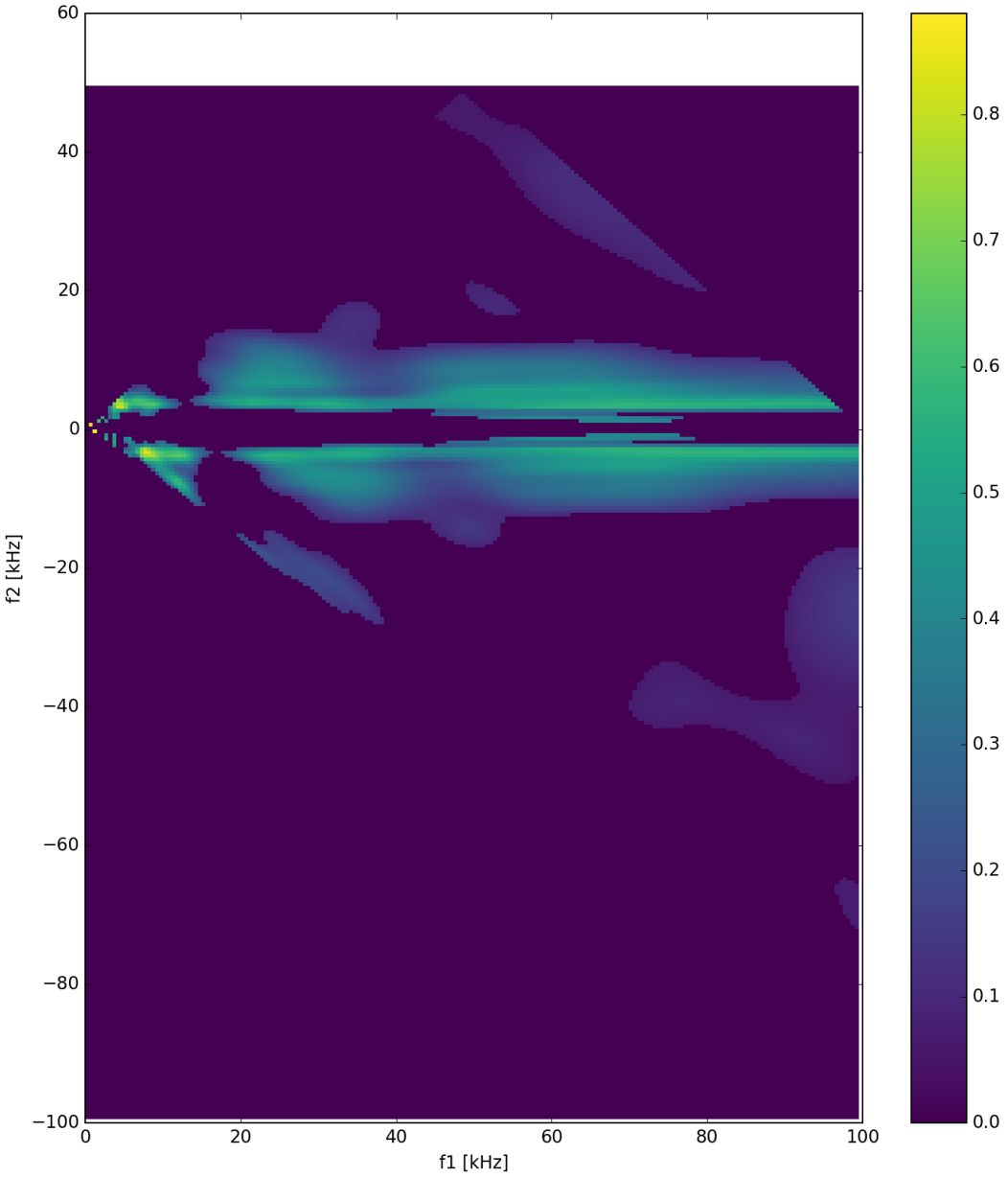

Figure 3: Bicoherence calculated in a time slice where LCO-like oscillations occurred in discharge 9617. A clear interaction with the ~ 3 kHz mode is seen. Only bicoherence below the estimated level of statistical noise is shown.

To display the time evolution of bicoherence so called summed bicoherence can be defined

which represents the average of bicoherence with any other modes

$$b(f) = \frac{1}{N(f)} \sum_{f=f_1+f_2} B_{xx}(f_1, f_2) \tag{2}$$

where $N(f)$ is the number of terms in the sum. The evolution of $b(f)$ from calculated B_{xx} on segments of length 2 ms is shown in Figure 4. The bicoherence of the $\sim$ 3 kHz mode is seen during the LCO-like oscillations. The frequency even seems to decrease towards 3 kHz in the second burst of oscillations. The two large peaks at the end have a different bicoherence characteristic and this may suggest that these are actually type III ELMs.

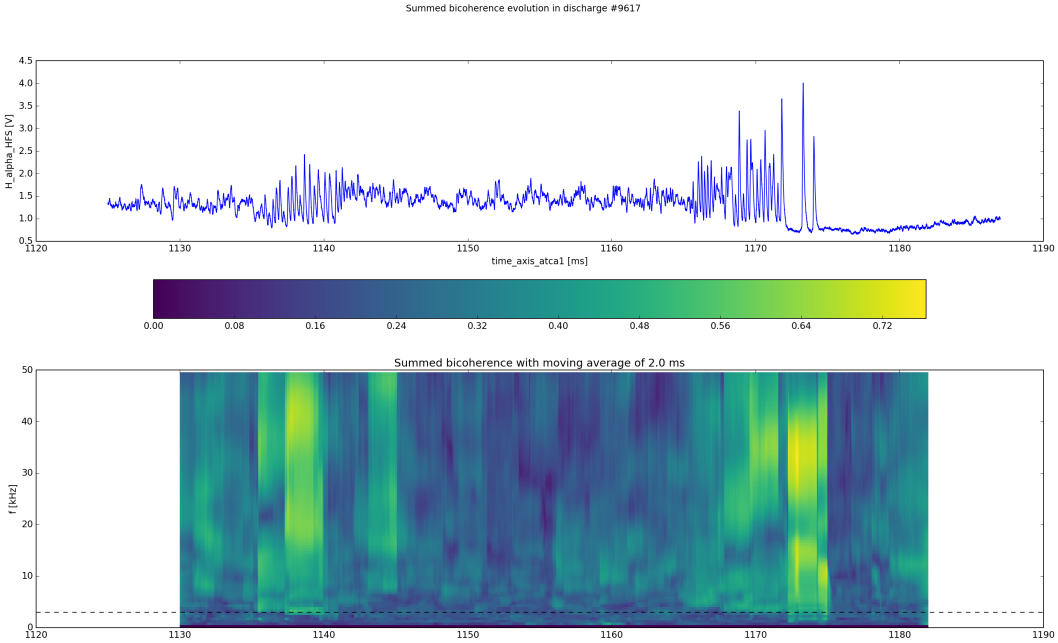

Figure 4: Evolution of summed bicoherence calculated in segments of length 2 ms in discharge 9617. The dashed line shows the 3 kHz mode and clear bicoherence is seen during the LCO-like oscillations.

3 Estimation of E_r with a conditional-averaging-like approach

Conditional averaging is an approach used to detect several occurrences of one type of an event and after aligning time traces of such an event an average waveform can be found by averaging the aligned points[7]. A similar approach was used to find E_r for the floating potential $\approx \phi$ of BPP1 in discharge 9617 shown in Figure 1 by aligning points of ϕ according to the phase of fluctuations and then taking a derivative of these points which due to reciprocation should correspond to a spatial derivative.

The main idea was to detect turbulent events in I_{sat} that could form time sections at which to take $\phi \approx V_f$. Averaging over a few ϕ sections could give a reasonable approximation of ϕ with turbulent time scales averaged out. Successive differences of ϕcould then give an prroximation of E_r with a reasonably high temporal resolution. The derivative and averaging

were be done in one step with a Savitzky-Golay filter, however, a linear interpolation of the SG filtered signal was then used to get equidistant time spacing.

To gain a temporal resolution sufficient to analyze LCO-like structures with $f \sim 3$ kHz and a phase shift of about $\frac{\pi}{2}$ between E_r and δn_e it is necessary to detect events with a sufficiently high frequency. With a requirement of at least 10 point per period to gain reasonable phase resolution a minimum frequency of 120 kHz was required. Visible oscillations of about 127 kHz frequency (most powerful spectral component) were found in the I_{sat} signal on LP2 as shown in Figure 5.

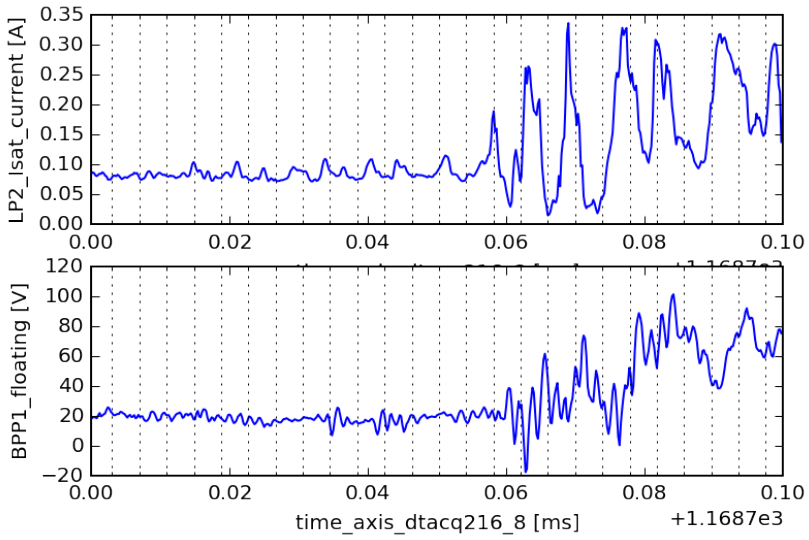

Figure 5: Fluctuations of I_{sat} and V_{fl} in discharge 9617 measured by the reciprocating probe. Oscillations of ~ 127 kHz were found which could be used a event markers.

The time domain evolution shown in Figure 5 seems to suggest there are fluctuation maxima at about the frequency of the maximum spectral component during large fluctuations, during the less fluctuating parts the frequency of maxima is almost double. The double frequency could be mitigated (in order to have more equidistant time deltas) by only taking maxima/minima appart at least a half period of the maximal spectral component.

Also, it is not clear whether maximia or minima are more consistent. It almost looks as if the minima are better, because it seems V_f goes close to or below 0 during the I_{sat} maxima and on the other hand V_f seems to have maxima during I_{sat} minima. This may be because of some correlation lag due to structures moving past the probe head rather than some fluctutation dynamics. For these reasons the minima were chosen as even phase markers.

Taking V_f sections corresponding to I_{sat} minima shows localized rises in the potential in the first two plots in Figure 6. As the sections are quite close to being equidistant a linear, 7 point Savitzky-Golay filter is applied to get an approximation of the successive differences $d\phi$ which are proportional to the E_r estimate. As only the phase of the estimate is important to determine any phase difference, multiplicative constants are neglected. The filtered signal was interpolated with a cubic spline to get a fully equidistant estimate. The envelope of density fluctuations δn_e was estimated as a lowpassed absolute value of the differences of the I_{sat} signal.

The δn_e envelope fluctuations appear to have a maximum when $d\phi$ crosses 0. This suggest

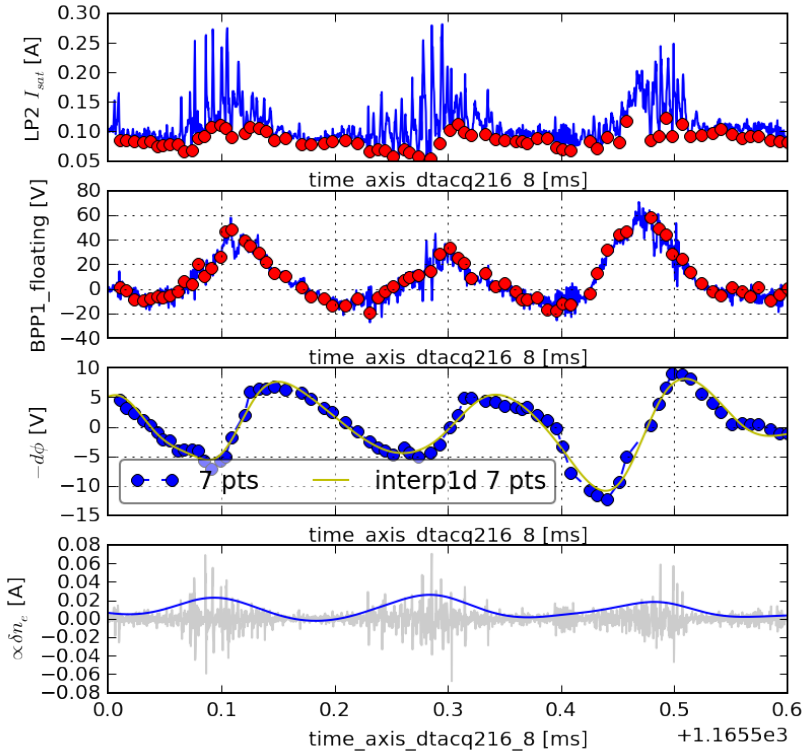

Figure 6: Fluctuations of I_{sat} and V_{fl} in discharge 9617 with local I_{sat} event markers shown by red points. The potential difference estimate and fluctuation envelope are shown in the two other plots.

a phase difference between the two signals close to $\frac{\pi}{2}$. The phase difference was estimated using Hilbert analysis from the analytic signals corresponding to the fluctuation signals. The comparison of H_α radiation and the phase difference estimate shown in Figure 7 suggests that there is a phase difference between $\pi/2$ and π during the LCO-like oscillations.

The observed phase difference suggests that these might be predator-prey dynamics observed in [8]. However, the nature of the reconstructed E_r oscillations is different that taht observed in HL-2A, where only a rise in the value of E_r was observed. This may be due to the reciprocating movement of the probe which simultaneously scans the possibly sheared E_r field.

4 Design of probe head for measurements of LCO

In order to perform similar experiments as in HL-2A [8] aimed at identifying the suspected modes as LCO it is necessary to obtain such a diagnostic which can measure the following quantities: Fluctuations of the electron density n_e (which are assumed to be a sign of turbulence strength) and the radial component of the electric field E_r which through the sheared $E \times B$ drift velocity acts to reduce the turbulence strength.

While the fluctuations of n_e can be readily measured by a Langmuir pin biased to measure the ion-saturated current, measuring E_r with high temporal resolution poses a much greater

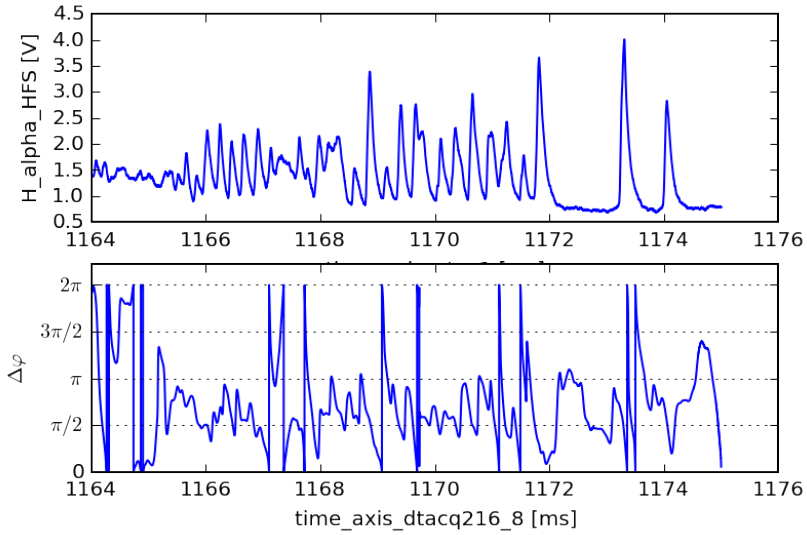

Figure 7: Comparison of H_α radiation evolution whong LCO-like oscillations and the phase difference between the I_{sat} difference envelope fluctuations and the potential difference estimate.

challenge. Following the unsuccessful estimation of E_r using the standard horizontal reciprocating manipulator probe head described in the previous thesis [4] modified designs based on this standard probe head were tested.

The two modified designs differ essentially only in the radial positions of BPPs. Their difference was in the order of several mm which was expected to yield the desired results. The different radial positions were achieved by cutting the graphite bulk base in order to create radial steps and the BPPs were retracted further into these steps to maintain the original depth of the BPP pins. The first design with 2 radial step separated by 5 mm is described and discussed in subsection 4.1. The second design with one central step is discussed in subsection 4.2.

However, these designs also proved to be unsuccessful and a completely new probe head design was created. This design features BPPs and LPs in similar spatial configurations which should enable a comparison of spatially resolved measurements using the two different probe types, e.g. the radial and poloidal components of the electric field and from them an estimate of the Reynolds stress. This design and first measurements with this new probe head are discussed in subsection 4.3.

4.1 Probe head with 5 mm steps

A modified version of the standard probe head was installed on the reciprocating manipulator in the COMPASS tokamak in September 2015. This new rake-like probe head featured 2 steps in the radial direction as pictured in figure 8. The steps were constructed by simply cutting off pieces of the standard graphite bulk base and retracting the probes further inwards to maintain the same level of shielding.

LCOs were measured on the HL-2A tokamak using a similar 3-step (in the radial direction) Langmuir probe (LP) array with 15 tips. Table 1 compares the geometry of the LP array

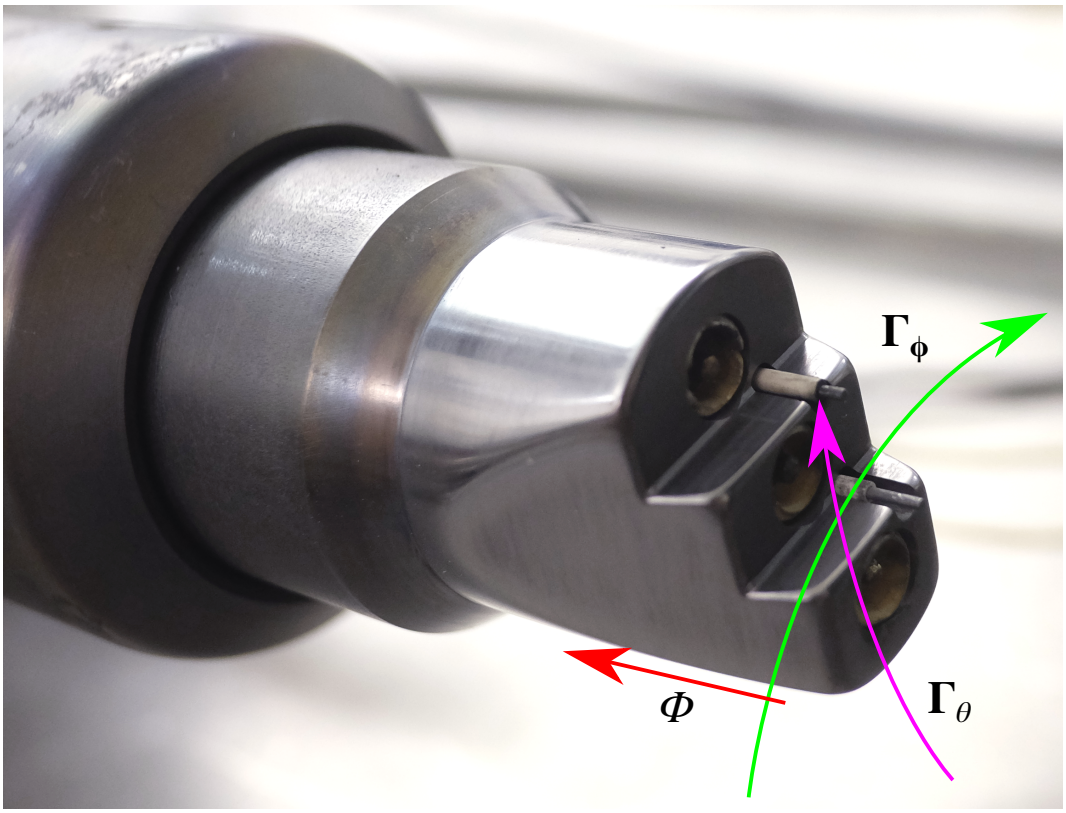

Figure 8: Schematic of the new Rake-like probe head installed in COMPASS in September 2015 with 5mm radial steps. Indicated are the toroidal and poloidal fluxes Γ_ϕ, Γ_θ which may be shielded due to the construction of the head and possible proliferation of the electric potential ϕ through the graphite layer.

(pictured in Figure 9) used on HL-2A with the 5 mm step BPP-Rake head in terms of the head's geometry.

Table 1: Comparison of the geometry of the HL-2A LP array and 5 mm step BPP-Rake heads.

attribute	HL-2A LP array	COMPASS BPP-Rake
steps (radial)	3	2
ΔR resolution [mm]	3	5
ΔZ resolution [mm]	5	8
max. reciprocation speed [m/s]	1	1
steady in max. [ms]	80	2?
max. inside separatrix [mm]	6	?

It is evident that the HL-2A LP array has a higher spatial resolution, both in the radial and poloidal directions (R and Z orthogonal coordinates on mid-plane). However, according to [2] the radial component of the electric field fluctuation used for calculating Reynolds stress was calculated using pins 1 and 6 (see Figure 9) which are separated by 6 mm radially and 10 mm poloidally. This spatial resolution is quite close to that available with the BPP-Rake

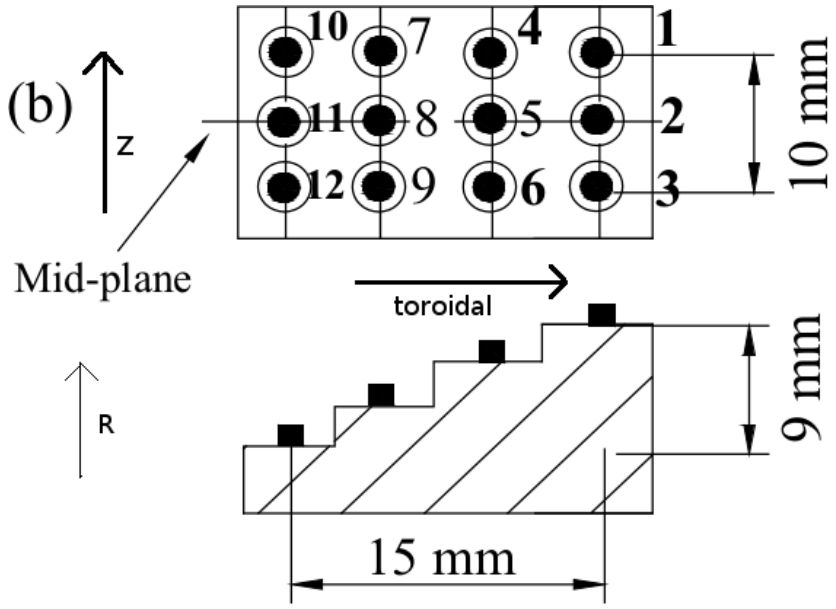

Figure 9: Geometry of the LP array head used on HL-2A for LCO measurements. Extracted from [2] and edited (added orthogonal mid-plane coordinates).

head. Nevertheless, the pins used for calculating the E_r signal used for LCO identification are not directly specified in [2]. It is also unclear how exactly was the radial component calculated using those pins and to what extent does the calculated signal represent the actual radial electric field.

If E_r was calculated using the same pins, then the BPP-Rake might offer sufficient resolution. A difference is also the fashion in which reciprocation is conducted. The LP array is inserted at a similar speed as in the case of BPP-Rake head, but it remains deeper inside the magnetic separatrix for a significant amount of time.

However, measurements of floating potentials in L-mode discharges 10923 and 10924 during the CC13.01 Runaway campaign in October 2015 have shown that the BPPs shielded by the probe head bulk are influenced in some unknown way which results in the maximums of the radial profiles of floating potentials to be radially shifted in the order of a few mm and the maximums not having the same height as can be see in Figure 10.

The difference between the maximums is $\sim$ 10 V. BPP3 and LP2 are the radially most inwards (most to the right in Figure 8) and they appear to have similar radial profiles of the floating potential during the outward reciprocation when LP2 was self-emissive and thus is expected to measure $V_{fl} \approx \phi$ as does BPP3. This suggests that BPP3 measures the correct floating potential and the other BPPs measure lower values due to shielding, likely due to to shielding of the poloidal flow Γ_θ as indicated in Figure 8. However, the radial shift in the position of the maximums suggests that the potential measured by BPP3 is partially proliferated to the other BPPs and thus they appear to measure the maxima at different radial positions. One possible explanation would be the proliferation of the plasma potential ϕ through the graphite layer as indicated in Figure 8.

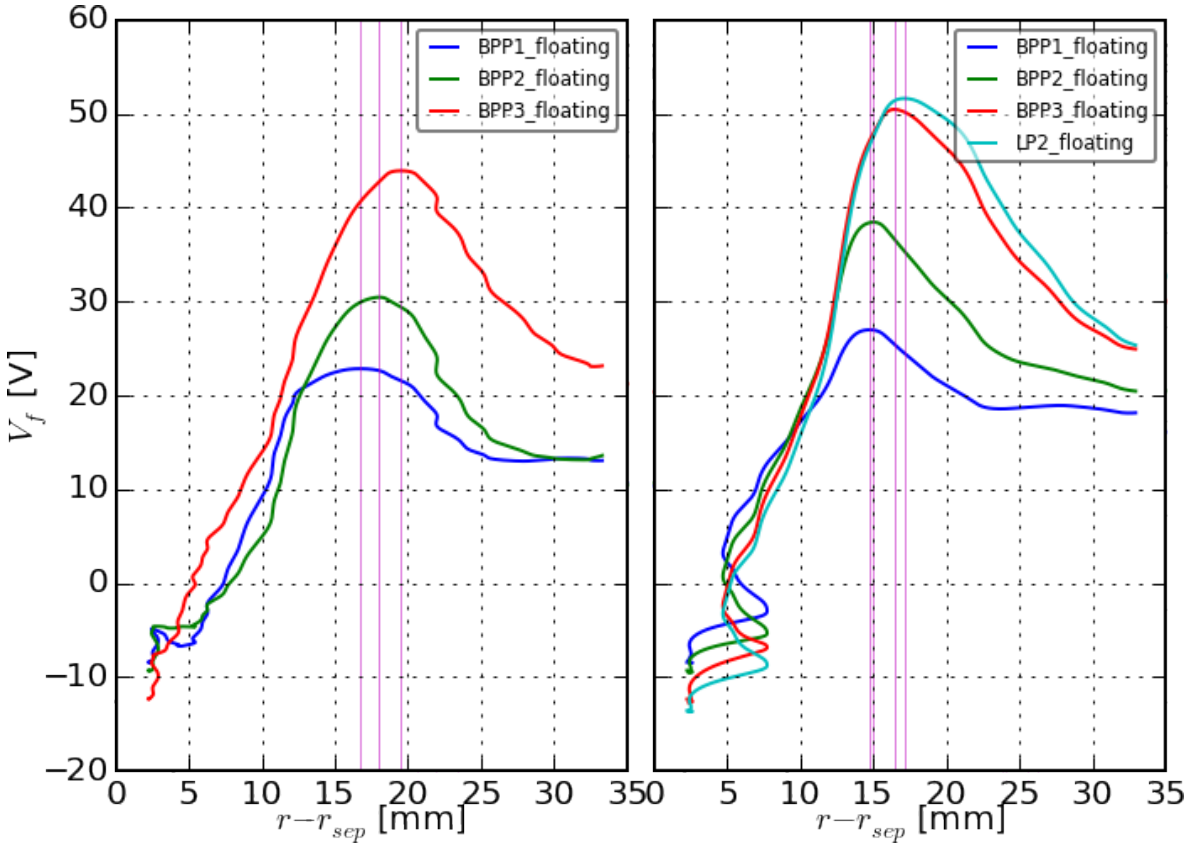

Figure 10: Floating potentials measured by probes on the 5mm step BPP-Rake probe head during the inward (left) and outward (right) reciprocation in discharge 10924. Vertical lines indicate the positions of maximums. During the outward reciprocation the LP2 probe became self-emissive and measure a floating potential close to BPP3.

4.1.1 Considerations for the next probe head design

The choice of 5 mm steps was also taken under consideration. In order to test different differentiation lengths Δr the radial profile of the BPP3 signal in discharge 10760 was interpolated to a linear-spaced interval on the radial axis. The derivative of the signal was then calculated with the smallest possible Δr available and then for $\Delta r = 2, 3, 5$ mm to investigate the effect of the radial step in the calculation of the derivative. The radial profile of the radial opposite[1] electric field was approximated as the central difference of the floating potential

$$-E_r(r) = \frac{V_f(r + \frac{\Delta r}{2}) - V_f(r - \frac{\Delta r}{2})}{\Delta r}$$

All calculations were performed on lowpassed signals in order to mitigate the highpass effect of differentiation.

It is quite obvious from figure Figure 11 that $\Delta r = 5$ mm is indeed too large to get a reliable approximation of the slope when it is large. There seems to be some similarity between the

[1]The minus in $E_r = -\frac{dV_f}{dr}$ is put on the left-hand side to make it simpler to relate the shapes of the graphs in terms of the slopes

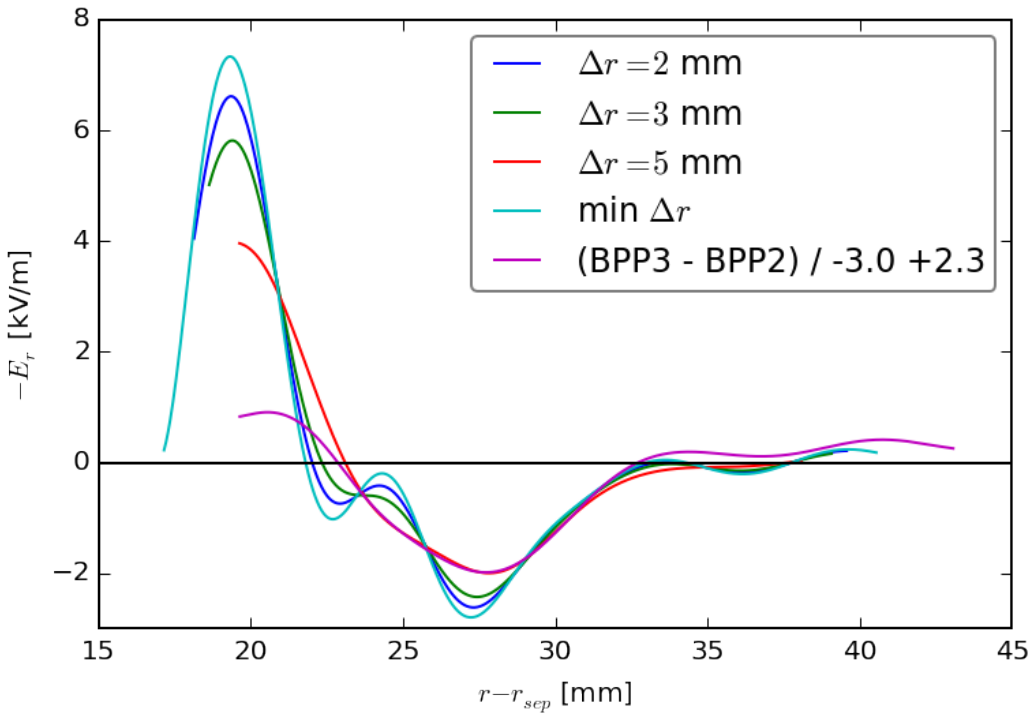

Figure 11: Results of differentiating with different Δr the interpolation of the radial profile of the BPP3 signal to a linear sampling in discharge 10760.

radial profile calculated with $\Delta r = 5$ mm and the difference of the two probe signals, but only after some linear transformation which seems to indicate that there is

- some unknown offset, possibly due to poloidal shielding
- a more elaborate projection of the field between the probes into the radial direction

However, this similarity holds only up to a certain depth.

Nevertheless, a choice of $\Delta r = 2$ mm seems small enough to get a reasonable approximation of the slope at higher values. However, the approximation will always give a slightly lower value for very rapid (in the r direction) gradients of the floating potential due to the finite spatial difference between the probes.

For the construction of a new probe head several different geometric configurations were considered in order to find a design optimized for the reconstruction of the various projections of the electric field between the probes.

Assuming the electric field between the probes is a linear combination[2] of a poloidal and radial field as shown in figure 12, three distinct options for the geometric configuration arise.

Variant A is the implementation of the 5 mm step design and offers only two linearly dependent directions, which makes it very hard to reconstruct the two projections. On the other hand, it is possible to measure differences at different radial positions, but that makes it even harder to use two differences to reconstruct the projections on the same position.

[2]This assumption likely won't hold in a curved field, but even in such a field that is stationary a linear combination of the projections should suffice as was derived in my bachelor thesis

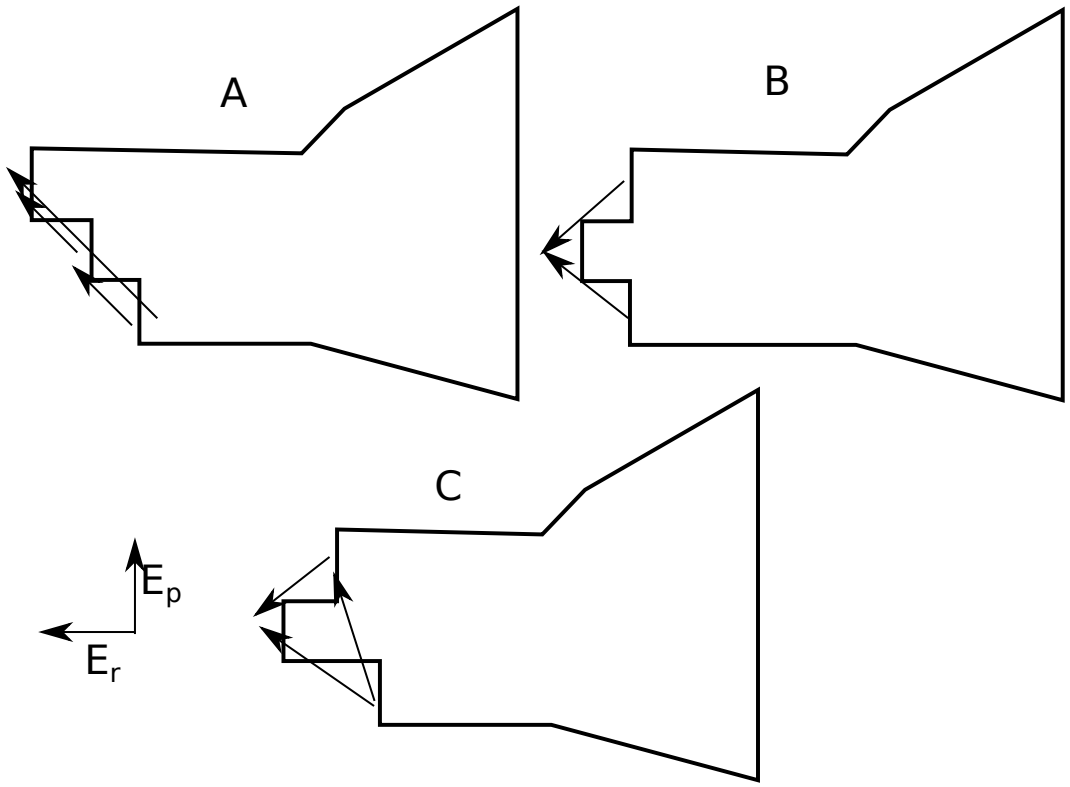

Figure 12: Possible geometric configurations of a BPP-Rake probe head. Arrows indicate electric field projections with respect to the poloidal and radial components of the electric field.

Variant B offers two orthogonal directions which makes it quite simple to calculate the projections of the electric field. Furthermore, the radial projection can be calculated on the same radial position. This is not possible with the poloidal projection though.

Variant C offers two linearly independent directions but also different radial positions.

It is also worth considering the effect of probe shielding by adjacent steps. In variants A and C one of the probes may be shielded by two steps, whereas in variant B each of the two potentially shielded probes is shielded only by one step.

Based on these considerations the next design was chosen to be based on variant B and to have just one 2 mm central step.

4.2 Probe head with central step

The second modified design of the standard HRCP probe head pictured in Figure 13 intended to use only one central step to get 2 linearly independent, perpendicular directions of field components which should simplify the extraction of the E_p and E_r components. Additionally, the step was made only 2 mm high in the radial direction in order to offer a high radial resolution for the E_r spatial derivative. Originally, the step was supposed to be made of graphite as a stub left by cutting off the side of the probe head. However, the central step fell off during processing so only the corundum shielding tube remained. This would have likely reduced any flux shielding by the steps. The absence of the graphite step could have also

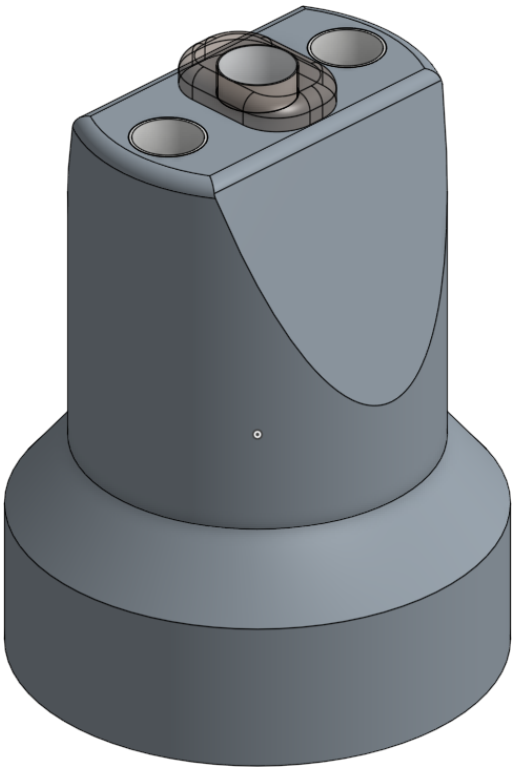

Figure 13: Schematic of the second BPP-Rake probe head design with one central 2 mm step in the radial direction. The graphite bulk of the step fell off durign material processing and the remaining corundum white insulation tube is indicated.

reduced the risk of the potential proliferation, however, corundum can become conductive as well under high thermal load[1], so the ϕ proliferation cannot be ruled out completely.

Additioally, the probe was rotated 45° around its main axis of symmetry (co-linear with the radial direction of reciprocation) to mitigate any possible effects of flux shielding by the central probe. Nevertheless, measurements of radial profiles of floating potentials in December 2015 in discharge 11412 showed the same deficiencies as those with the previous design described in subsection 4.1 as can be seen in Figure 14. The two radially further outward (on the sides in Figure 13) probes appear to have a systematic offset and the maximum of the floating potential is lower than with the center probe. They both appear to have a similar offset, which might indicate that their equal radial displacement results in the same effect. The maximums of the measured potentials were measured at almost the same time, corresponding to a displacement in the radial profile of 2 mm when the displacement of the center probe is accounted for. This "temporal synchronization" suggests that the issue of possible ϕ proliferation persists and may have been made even worse by moving the probes closer radially, resulting in almost perfect synchronization.

4.3 Design of a new probe head for E_r and Reynolds stress measurements

The failures of previous designs prompted a completely new design. This new design is based on previous discussions between Carlos Hidalgo, Martin Hron and Jiří Adámek about a probe

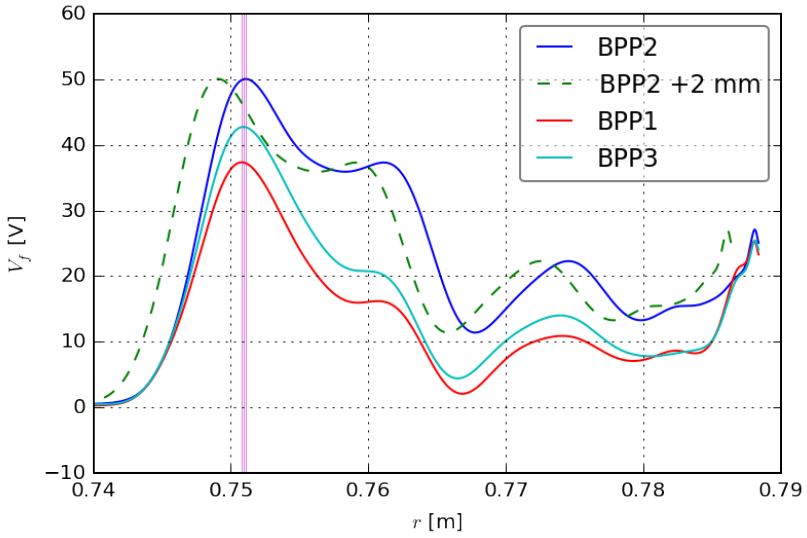

Figure 14: Radial profiles of floating potentials measured in discharge 11412 with the modified probe head design with the central 2 mm step. The BPP2 profile shows a maximum which would not correlate with the other probes if its radial displacement was accounted for.

head design for the COMPASS tokamak aimed at measuring Reynolds stress $R_{r\theta}$. One of the components necessary for measurement and computation of $R_{r\theta}$ is E_r and thus the design is also suitable for LCO measurements.

The key feature of this design is the simultaneous usage of both BPPs and LPs for each kind of measurement which makes it possible to compare results obtained with BPPs with the standard approach using LPs. Therefore, any physically significant measurements of V_f with BPPs (which are likely closer to ϕ and thus may have high physical significance) can gain more trust when compared with the more common methods involving LPs. There are also several different ways to measure and calculate e.g. E_r, E_p from different combinations of probes which enables cross-validation of results.

A significant change in comparison with previous designs is the use of boron nitride instead of graphite as the material for the main head bulk in which probes are fixed. The main motivation is that boron nitride does not have such conductive properties which graphite or corundum under high heat loads may have. Therefore, it is less likely to electrostatically affect the surrounding plasma or the measurements of V_f as may have been the case with the previous probe head designs.

The distance between tips of adjacent probes is minimized to 4 mm on average with the main constraints being the thickness of the material between them and flow screening due to $E \times B$ drifts. The probes closest to each other are arranged in a pattern close to a triangular mesh as can be seen in Figure 15.

The probe head contains 5 BPPs and 6 LPs. The BPPs tips are embedded 0.5 mm below the head bulk surface and are contained in a cylindrical cavity with a diameter of 2 mm and a height of 3 mm (see Figure 15). The tips of LPs protrude 1.5 mm above the head bulk surface. In cases where LPs are shielded by a material wall from a certain direction the wall extends by 1 mm above the LP tip. The protrusion length of LP tips and the shielding wall extension results in the lowest possible radial separation of 2.5 mm between measurements for

each probe type.

Probes are named `{X}P{N}`, `X` being one of `BP` or `L` and `N` being a number assigned for each probe type separately in a top to bottom, left to right order.

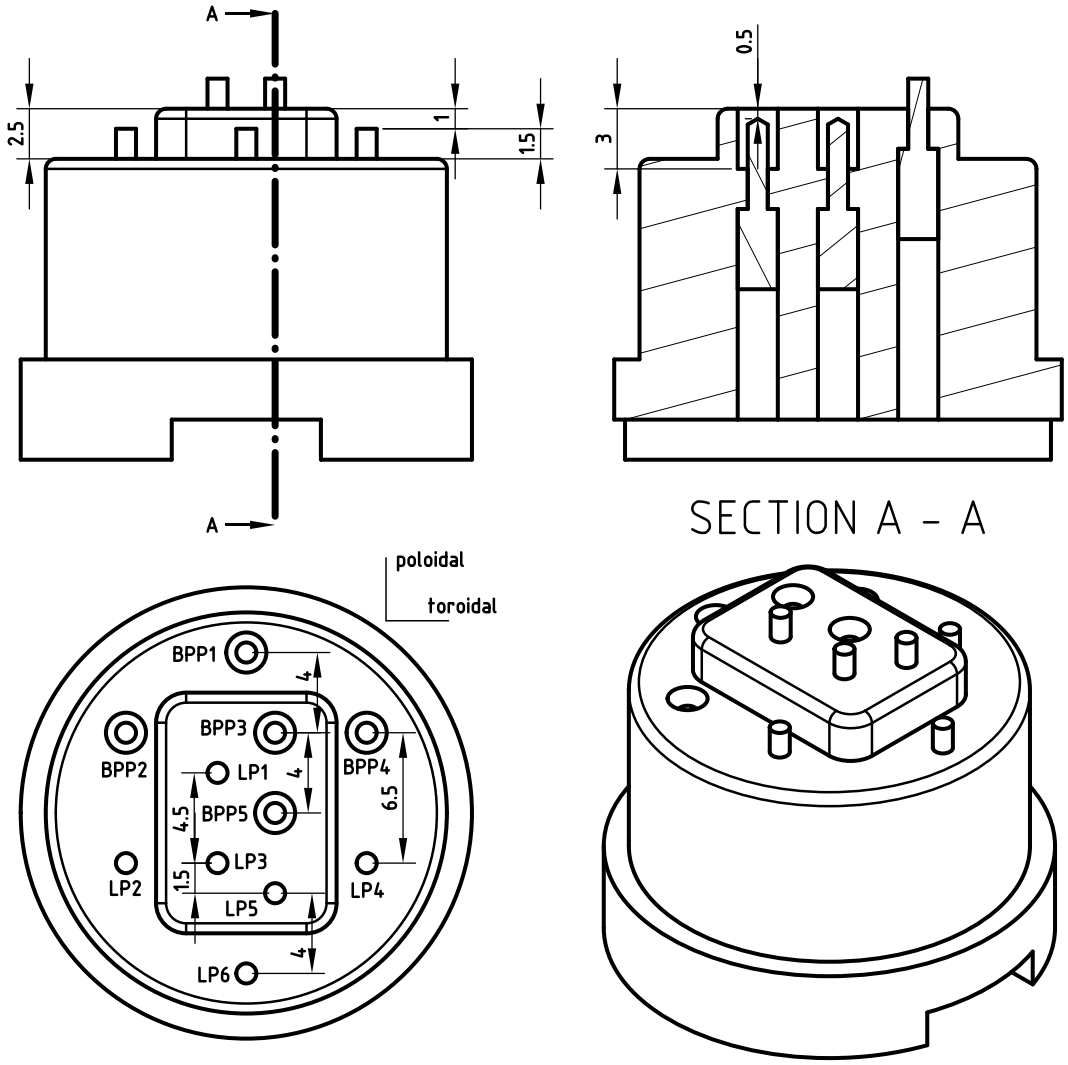

Figure 15: Schematic of main probe head bulk with probes. Dimensions are in mm. Only physically relevant dimensions are included.

4.3.1 Overview of different measurement of selected physical quantities

In this section a brief overview of different possible measurement setups for selected physical quantities is given. Quantities most relevant to LCO and turbulence measurements are selected.

4.3.2 Electron temperature T_e

Estimation of T_e with high temporal resolution and its radial profile (due to reciprocation) is possible by measuring the difference between floating potentials of a BPP and LP positioned

close to each other. For this purpose a combination of LP1 and BPP3 or BPP5 is likely optimal.

4.3.3 Poloidal electric field E_θ

The simplest estimate of E_θ is the difference of floating potentials measured by BPP3 and BPP5 (respectively LP3 and LP5) divided by the distance of their tips. Neglecting the slight toroidal separation between LP1 and BPP3, BPP5 it is also possible to cross-check with the difference between LP1 and one of these probes, assuming T_e is measured with some other combination of probes and assuming T_e does not significantly change over the distance between the probes.

4.3.4 Radial electric field E_r

The two probe head levels separated radially by 2.5 mm enable radially separated measurements of floating potentials either with BPP or LP. To obtain only E_r, it would be optimal to perform measurements which are separated only radially and not poloidally or toroidally. Unfortunately, this is not possible due to the construction of the probe and the use of BPPs which require positioning perpendicular to B_ϕ. Toroidal separation is assumed to be insignificant due to dominant toroidal flows. Therefore, BPP3 (respectively LP3) is chosen as one of the measurement points and the second one has to be reconstructed from probes on the lower level.

One option is to assume that the average of floating potentials measured by BPP2 and BPP4 (respectively LP2 and LP4) is a reasonable estimate of the floating potential halfway between them, because they are each affected by a mutually complement, dominantly toroidal flow from one of their sides. The placement of this estimate puts it under BPP3 with no poloidal separation and negligible toroidal separation. The estimated E_r is then the difference between V_f measured by BPP3 and this average potential divided by 2.5 mm.

A second option is to assume that the difference between floating potentials measured by BPP1 and BPP3 (respectively LP5 and LP6) is an estimate of $\left(\vec{E}_r + \vec{E}_\theta\right) \cdot \vec{l}$ and with and estimate of E_θ the radial field can be extracted since the separation vector between the probe tips $\vec{l}$ is known from the probe geometry.

A third option useful mostly for comparison with the previous options is to estimate E_r from the radial profiles of the floating potential as the derivative. However, this method gives an estimate with a low time resolution, because high frequencies would be amplified by differentiation.

4.3.5 I sat, density, flow

Langmuir probe tips with sufficient biasing can measure the ion saturated current I_{sat} and by combining with measurements from different probes (T_e, $\vec{E}$) other quantities, for instance n_e and $\vec{\Gamma}$ can be deduced.

4.4 Commissioning of the new probe head design

The new probe head was installed and first tested at the end of June 2016. First reciprocation tests in discharge 12174 showed that the previous design deficiencies were overcome as can be seen in Figure 16.

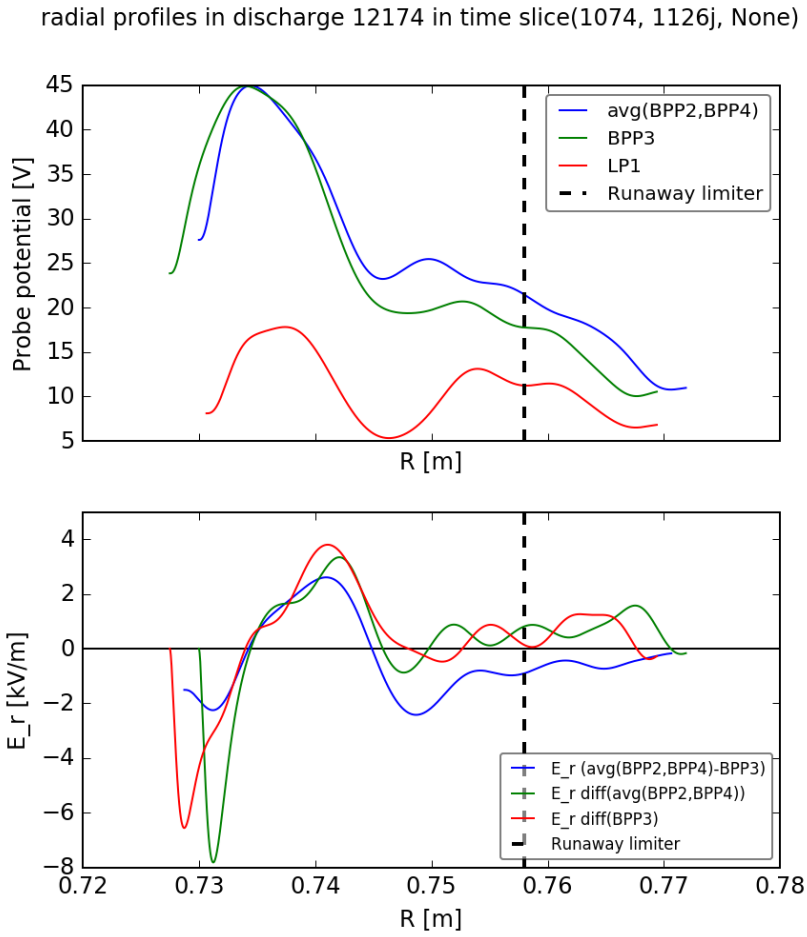

Figure 16: Radial profiles of floating potentials and estimated radial electric fields measured during the inward reciprocation in discharge 12174.

The maximums of the radial profiles of the floating potentials measured by the BPPs appear to have the same height and radial position. The average of the two partially shielded BPPs on the side also seems to give a good estimate of the floating potential at the position between them since the radial profiles coincide. There are some discrepancies further inwards, possibly due to saw-teeth which somewhat contaminated the results.

The radial electric field estimated from the difference of the floating potentials at each time instance appears to agree well with the low-time-resolution estimates obtained from the differentiation of the low-passed radial profiles of floating potentials at least for lower levels of E_r. For higher levels this method appears to give lower values, likely due to the limits of the spatial difference discussed in subsubsection 4.1.1.

4.4.1 Issues during commisioning of the new design

The probe was used several times after that during the CC15.04 campaign. However, during attempts at deeper reciprocation disruptions occurred close to the entry of the probe head into the LCFS as seen in Figure 17

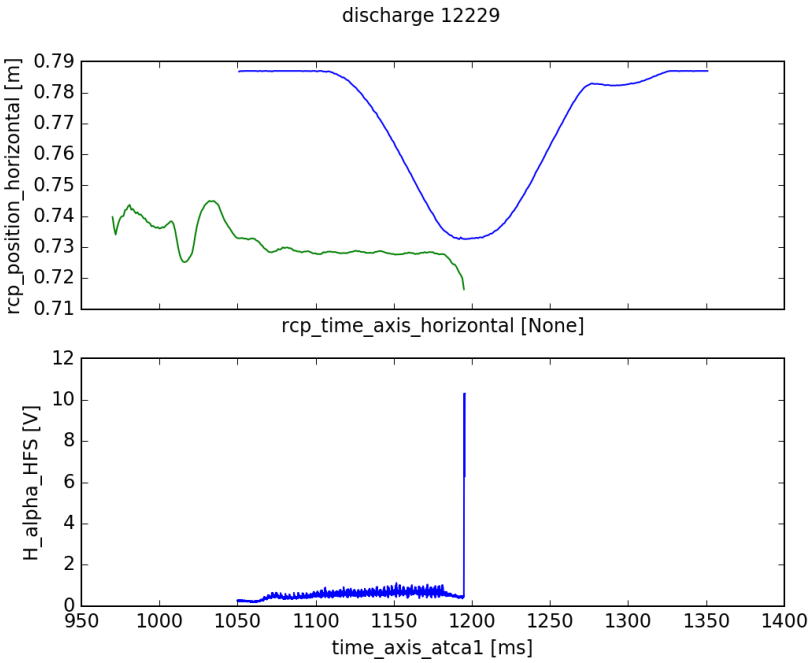

Figure 17: Evolution of the radial position of the probe (blue line in top plot) and the position of LCFS (green line) and the H_α radiation from plasma in discharge 12229 shows a disruption upont the netry of the probe close to the LCFS.

This was likely due to the out-gassing of residual gas in the boron nitrite bulk head. It is possible that this will be reduced if the probe is used in more experiments and remaining gas will be eventually eliminated. This process could be also expedited by baking the probe in an appropriate vacuum oven if one is procured.

However, visual inspection of the probe after the experiments has also shown that some edges of the boron nitrite bulk have been damaged, likely by sputtering as can be seen in Figure 18. This has indicated that the life-expectancy of the probe head may be lower than previously thought and only a limited number of experiments will be possible.

5 Conclusion

The spectral characteristics of the LCO-like oscillations were investigated and a corresponding coherent $n = 0$ magnetic mode has been found. The oscillations around 3 kHz were also found to exhibit bicoherence with a broad band of frequencies.

An attempt was made to reconstruct the radial electric field E_r using a method similar to conditional averaging. This approach yielded an estimate which suggests that there is a phase difference close to $\pi/2$ between the amplitude of the density fluctuations and the strength of E_r which points to predator-prey-like dynamics.

Several designs of a probe head for the horizontal reciprocating manipulator were tested. The first two designs were modified versions of the standard probe head design with radial steps. A completely new design for a probe head has been made which featured many more smaller BPP and LP probes. This design appears to successfully measure E_r with high

Figure 18: Visual inspection of the probe after the CC15.04 campaing showed damaged edges of the boron nitrite bulk.

temporal resolution. However, the new probe head requires further testing to determine if the probe head is suitable for further measurements due to plasma-material interactions.

References

[1] A. E. Van Arkel, E. A. Flood, and Norman F. H. Bright. "The electrical conductivity of molten oxides". In: *Canadian Journal of Chemistry* 31.11 (1953), pp. 1009–1019. DOI: 10.1139/v53-133. eprint: http://dx.doi.org/10.1139/v53-133. URL: http://dx.doi.org/10.1139/v53-133.

[2] J. Cheng et al. "Low–intermediate–high confinement transition in HL-2A tokamak plasmas". In: *Nuclear Fusion* 54.11 (2014), p. 114004. URL: http://stacks.iop.org/0029-5515/54/i=11/a=114004.

[3] J. Cheng et al. "Low–intermediate–high confinement transition in HL-2A tokamak plasmas". In: *Nuclear Fusion* 54.11 (2014-11-01). ISSN: 0029-5515. DOI: 10.1088/0029-5515/54/11/114004. URL: http://stacks.iop.org/0029-5515/54/i=11/a=114004?key=crossref.f37b6a1d0052f5eda573db228e502124.

[4] Ondřej Grover. *L-H přechod a H-mód v tokamakovém plazmatu: bakalářská práce*. Praha: ČVUT, FJFI, Katedra fyziky, 2015.

[5] B. Ph. van Milligen et al. "Wavelet bicoherence: A new turbulence analysis tool". In: *Physics of Plasmas* 2.8 (1995), pp. 3017–3032. DOI: http://dx.doi.org/10.1063/1.871199. URL: http://scitation.aip.org/content/aip/journal/pop/2/8/10.1063/1.871199.

[6] Christopher Torrence and Gilbert P. Compo. "A Practical Guide to Wavelet Analysis". In: *Bulletin of the American Meteorological Society* 79.1 (1998), pp. 61–78. DOI: 10.1175/1520-0477(1998)079<0061:APGTWA>2.0.CO;2. eprint: http://dx.doi.org/10.1175/1520-0477(1998)079<0061:APGTWA>2.0.CO;2. URL: http://dx.doi.org/10.1175/1520-0477(1998)079%3C0061:APGTWA%3E2.0.CO;2.

[7] Petr Vondráček. *Studium okrajového plazmatu tokamaku COMPASS pomocí dvojice reciprokých sond*. Diplomová práce. Praha, 2012.

[8] Y. Xu et al. "Dynamics of low–intermediate–high-confinement transitions in the HL-2A tokamak". In: *Plasma Physics and Controlled Fusion* 57.1 (2015), p. 014028. URL: `http://stacks.iop.org/0741-3335/57/i=1/a=014028`.